Phonon mechanism explanation of the superconductivity dichotomy between FeSe and FeS monolayers on $SrTiO_3$ and other substrates

Baruch Rosenstein [1,*] and B. Ya. Shapiro [2,†]
[1] *Electrophysics Department, National Yang Ming Chiao Tung University, Hsinchu 30050, Taiwan, Republic of China*
[2] *Physics Department, Bar-Ilan University, 52900 Ramat-Gan, Israel*

(Received 8 February 2021; revised 14 May 2021; accepted 2 June 2021; published 14 June 2021)

It was observed recently [Shigekawa *et al.*, PNAS **116**, 2470 (2019)] that while monolayer iron chalcigenide FeSe on a $SrTiO_3$ (STO) substrate has a very high critical temperature, its chemical and structural twin material FeS/STO has a very low T_c, if any. To explain this, the substrate interfacial phonon model of superconductivity in iron chalcogenides is further developed. The main glue is the oxygen ion $\Omega_s = 60$ meV vibrations longitudinal optical (LO) mode. The mode propagates mainly in the TiO_2 layer adjacent to the monolayer (and also generally present in similar highly polarized ionic crystals like $BaTiO_3$, rutile, and anatase). It has stronger electron-phonon coupling to electron gas in FeSe than a well-known $\Omega_h = 100$ meV harder LO mode. It is shown that while (taking into account screened Coulomb repulsion effects) the critical temperature of FeSe on STO and TiO_2 is above 65 K, it becomes less than 5 K for FeS due to two factors suppressing the electron-phonon coupling. The effective mass in the latter is twice smaller and, in addition, the distance between the electron gas in FeSe to the vibrating substrate oxygen atoms is 15% smaller than in FeS, reducing the central peak in electron-phonon interaction. The theory is extended to other ionic insulating substrates.

DOI: 10.1103/PhysRevB.103.224517

I. INTRODUCTION

Several years ago, a group of 2D high T_c superconductors ($T_c > 65$ K) was fabricated by deposition of a single unit cell (1UC) layer of FeSe on insulating substrates $SrTiO_3$ (STO) [1], TiO_2 (both rutile [2] and anatase [3]), and [4] $BaTiO_3$. The 3D parent iron chalcogenides (Se, S, Te) are unconventional superconductors ($s^{\pm}$ wave symmetry) with modest $T_c = 5-10$ K. Band structure (including both the hole band around the Γ and an electron band at the M point) is similar to that of iron pnictides, suggesting an unconventional spin fluctuation (SF) pairing mechanism [5] within the FeSe layer. Despite the fact that in 1UC FeSe/STO, the Γ band is missing, similar theories were constructed [6]. In addition, the strong $^{16}O \rightarrow {}^{18}O$ isotope substitution effect [7] indicates that superconductivity is at least enhanced by the electron-phonon interaction (EPI) [8–11].

Incipient band models of high T_c in FeSe monolayers that incorporate the phonon pairing (boosting T_c) up were constructed [11,12]. The EPI is represented by an interfacial mode of high frequency $\Omega = 100$ meV, close to that of the Fuchs-Kliewer modes (FK) observed via high-resolution electron energy loss spectroscopy [13]. The FK are vibrations of the substrate oxygen atoms in the direction z perpendicular to the interface, see the blue arrow in Fig. 1. The EPI strength $\lambda = 0.1$ turned out to be sufficient [11] to enhance the incipient band theory value of $T_c = 47$ K to $T_c = 65$ K. If the SFs were switched off (zero on-site repulsion, $U = 0$), one would require at least $\lambda = 0.2$ (consistent with previous purely phononic calculations of Ref. [8]). This implies that the SF contribution to pairing in the present case might be subdominant. This statement is not at odds with the understanding that superconductivity in bulk FeSe or FeS is due to SF, since there are two major differences between the bulk and 1UC. First, the hole band at Γ in bulk is missing and, second, the spin susceptibility measurement [14] from the bulk to monolayer FeSe signal of the spin is completely different.

Recently, the second monolayer iron chalcogenide, FeS, on STO was synthesized [15] by the topotactic reaction and molecular-beam epitaxy. In both iron chalcogenides, the Fermi surface consists of two nearly coincident pockets around the M point of the Brillouin zone, while the electron pocket at the Γ point of the parent materials sinks [16] (about 80 meV) below Fermi level. Despite the fact that (i) the bulk T_c, (ii) the 2D electron gas (2DEG) including spin dynamics, and (iii) EPI in FeSe and FeS are quite similar; surprisingly, superconductivity in FeS/STO was not observed [15], at least at temperatures above 10 K. This came as a surprise and even was termed by the authors "a dichotomy" that "strongly suggests that the cross-interface electron–phonon coupling enhances T_c only when it cooperates with the pairing interaction inherent to the superconducting layer." This interpretation rules out theories in which the EPI is the major cause of the tenfold enhancement of T_c in FeSe/STO.

However, despite the above superficial observations, there are two important differences between the two monolayers. First, the angle-resolved photoemission spectroscopy (ARPES) measurement [15] clearly demonstrates that the effective mass m^* is twice larger in FeSe than in FeS. In addition, the scanning transmission electron microscopy

*vortexbar@yahoo.com
†shapib@biu.ac.il

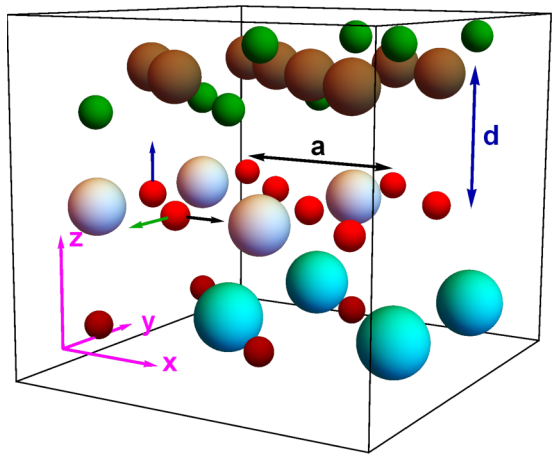

FIG. 1. Interfacial phonon modes. Oxygen ion's vibrations in the TiO_2 substrate layer Ti, silver; O, red). The displacement in direction perpendicular (z axis, blue arrow) to the one unit cell thin Fe (brown)-chalcogenide (Se, S, Te—green) layer are associated with FK modes. The two modes most relevant for the phonon-mediated pairing longitudinal optical modes are the Ti–O stretching mode (shown by black arrow) and the Ti–O–Ti bending (dark green arrow). The next layer Bi (cyan)–O (dark red) influencing the interfacial phonon frequency is also shown. Direction of propagation of the vibration wave is assumed to be along the x direction.

image of FeS/STO reveals the distance from the 2DEG gas in FeS to the vibrating substrate oxygen atoms, see Fig. 1, is $d = 5.3A$, larger than the corresponding distance [17] in FeSe/STO, $d = 4.6A$. These two observations are in direct contradiction with statement (iii) above that the EPI is similar in two systems. Indeed, since the EPI has a central peak in scattering (SCP) that exponentially depends on d, one would expect reduced EPI strength λ in FeS. The density of states in 2DEG is m^*/π, also reducing λ in FeS. On the contrary, if the in-plane SF mechanism of pairing is similar and dominant, absence of superconductivity in FeS/STO poses a problem for this explanation.

In this paper, the dichotomy between the iron chalcogenide monolayers FeSe and FeS is addressed theoretically in the framework of the dominant phonon mechanism. An interfacial phonon is considered as the dominant superconductivity glue overcoming (the screened) Coulomb interaction. The relevant phonon mode is the oxygen ion vibrations in the interface layers. The role of the insulating substrate therefore clearly extends beyond the efficient monolayer charging [18]. The dichotomy between superconductivity in FeSe/STO and FeS/STO is therefore resolved within this framework. In addition, more general systems with arbitrary effective masses m^*, the 2DEG layer-substrate spacing d and various substrates (characterized mostly by the dynamic dielectric constant) are considered.

II. MODEL

In recent theoretical investigations of superconductivity in one-layer FeSe on the STO substrate, the spectrum near the Fermi surface is described by the five-band model [19,20], similar to the description of bulk FeSe and other iron pnictides and chalcogenides [21]. In this approach, electrons in the FeSe layer hop largely between the nearest Fe atoms. Despite the fact that the system's unit cell with lattice spacing a, see Fig. 1, contains two iron atoms, one can effectively use a smaller unit cell rotated by 45° with spacing $a' = a/\sqrt{2}$ (see picture and definitions in Appendix A). Not all five Fe $3d$ bands ($d_{xy}, d_{xz}, d_{yz}, d_{x^2-y^2}, d_{3z^2-r^2}$) present within 2 eV near the Fermi surface in DFT calculations [20] are important for superconductivity. Since the hole pocket near the Γ point of the Brillouin zone (BZ) is located 80 meV below the Fermi level, one is left with a single electron band.

The minimal one-band model and parameters fitted from the ARPES measurement [15] are described in detail in Appendix A. It is shown there that it is sufficient to use an effective mass approximation, $E_{\mathbf{k}} = k^2/2m^* - \mu$, to describe (to 3%) superconductivity within the weak coupling approach. Effective masses are $m^*_{\mathrm{FeSe}} = 3m_e$ and $m^*_{\mathrm{FeS}} = 1.5m_e$, while Fermi energies are $\mu_{\mathrm{FeSe}} = 60\,\mathrm{meV}$ and $\mu_{\mathrm{FeS}} = 30\,\mathrm{meV}$. The Fermi momentum, $k_F = \sqrt{2m^*\mu}$, therefore, is nearly the same.

The identification of the phononic glue is a delicate task [12]. It was noted long ago [22] that transverse modes (including the FK mode responsible for the replica band in ARPES experiments [23]) are generally unable to provide the pairing glue, so one has to concentrate on the longitudinal modes only. A multitude of both the bulk STO and the interface modes has been studied in the framework of the DFT [24]. A simple phenomenological model of ionic crystal allowed us [8] to identify two longitudinal optical (LO) surface modes that have the strongest coupling to 2DEG in the sense that their exchange produces effective attraction of electrons in the lateral ($x - y$) direction. These are the Ti–O stretching (along the surface, see black arrow in Fig. 1) mode comparable in energy to the FK, $\Omega^{\mathrm{LO}}_{\mathrm{st}} = 100\,\mathrm{meV}$, and a lower frequency Ti–O–Ti bending (still along the interface direction, see dark green arrow) mode $\Omega^{\mathrm{LO}}_b = 60\,\mathrm{meV}$. Their matrix elements with the 2DEG electrons are about the same. All other modes (including phonons in the FeSe layer itself) have negligible matrix elements.

Since the phononic glue comes mostly from the TiO_2 substrate separated from the 2DEG by the (minimal) distance d, see Fig. 1, the EPI coupling exhibits the exponential forward scattering peak [10]:

$$g(\mathbf{k}) \approx \frac{2\pi}{a^2} e^{-kd}. \tag{1}$$

While in the minimal one-band model, the full form of the tight-binding matrix elements [8] is used [see Appendix A, Eqs. (A15) and (A16)], here the continuum limit is enough and considerably simplifies the calculations, making them semianalytic. The TiO_2 layer generally appears in all the substrates [17] (rutile, anatase, STO, $BaTiO_3$) as the first interface oxide layer (in addition to STO). The phonon exchange generate effective electron–electron attraction dynamic potential is

$$V^{\mathrm{ph}}_{\mathbf{k},n} = -\frac{(\mathrm{Ze}^2)^2}{M} \frac{g^2_{\mathbf{k}}}{\omega_n^2 + \Omega_s^2}. \tag{2}$$

Here M and $Z \simeq 1.27$ are the oxygen ion mass and the ionic charge, respectively [25], and $\omega_n = 2\pi T n$ is the bosonic Mat-

subara frequency. It was shown in Ref. [8] that the lower frequency bending mode ($\Omega_b^{\rm LO} = 60\,$meV) leads to larger $\lambda = 0.23$ than the stretching mode ($\Omega_{\rm st}^{\rm LO} = 100\,$meV) with $\lambda = 0.07$. Moreover, the bending mode pairing alone is strong enough to mediate high T_c above 47 K.

In view of the exponential SCP, Eq. (1), the EPI pairing in FeS/STO is weaker than in FeSe/STO since the distance between 2DEG and the TiO_2 layer increases [15] by 15%. This alone should reduce the EPI coupling. The reduced density of state also suppresses the EPI pairing. As a result of the two facts for the weaker pairing in FeS/STO, one should take into account the pseudopotential [26]. Coulomb repulsion in 2DEG (although effectively screened by the dielectric substrate [8] in both monolayers), might completely suppress superconductivity,

$$V^C_{\mathbf{k},n} = \frac{v^C_{\mathbf{k},n}}{1 - 2v^C_{\mathbf{k},n}\chi_{\mathbf{k},n}}, \quad v^C_{\mathbf{k},n} = \frac{2\pi}{\varepsilon(\omega_n)k}, \tag{3}$$

where the (Matsubara) dielectric function inside the substrate reads [11]

$$\varepsilon(\omega) = \frac{1}{2}\left\{1 + \varepsilon_\infty + (\varepsilon_0 - \varepsilon_\infty)\frac{\Omega_T^2}{\Omega_T^2 + \omega^2}\right\}. \tag{4}$$

Dielectric constants will be taken as follows. The optical value is rather universal for all the substrates (STO, rutile, and anatase), $\varepsilon_\infty = 5.5$, while the static ε_0 varies from as high as $\varepsilon_0 = 3000$ for $SrTiO_3$ to $\varepsilon_0 = 50$ for some anatase samples). The (bulk) transverse mode frequency appearing in Eq. (4) is estimated using the Lydanne-Sacks-Teller relation $\Omega_T = \Omega_{\rm LO}\sqrt{\varepsilon_\infty/\varepsilon_0}$ with $\Omega_{\rm LO} = 120\,$meV. The 2D Matsubara polarization function is

$$\chi_{\mathbf{k},n} = -\frac{m^*}{\pi}\{1 + 2\,\mathrm{Re}((1/2 + i\omega_n m^*/k^2)^2 - (k_F/k)^2)^{1/2}\}. \tag{5}$$

The sum of two competing contributions, the effective electron-electron interaction, $V_{\mathbf{k},n} = V^{\rm ph}_{\mathbf{k},n} + V^C_{\mathbf{k},n}$, determines the superconducting properties of these systems.

The scanning tunneling microscope (STM) experiments [27] demonstrate that the order parameter is gapped (hence no nodes) and indicate a weakly anisotropic spin singlet pairing. Therefore, we look for solutions for the normal and the anomalous Green's function of the Gorkov equations (derived for a multiband system in Ref. [8]), in the form $\langle\psi^\rho_{\mathbf{k},n}\psi^{*\sigma}_{\mathbf{k},n}\rangle = \delta^{\sigma\rho}G_{\mathbf{k},n}$, $\langle\psi^\sigma_{\mathbf{k},n}\psi^\rho_{-\mathbf{k},-n}\rangle = \varepsilon^{\sigma\rho}F_{\mathbf{k},n}$ (σ, ρ are spin components). In terms of the gap function,

$$\Delta_{\mathbf{k},m} = -T_c\sum_{\mathbf{p},n} V_{\mathbf{k}-\mathbf{p},m-n}F_{\mathbf{p},n}, \tag{6}$$

the linearized gap equation becomes (normal Green's function not renormalized significantly at weak coupling)

$$-T_c\sum_{\mathbf{l},m}\frac{V_{\mathbf{l},n-m}}{\left(\omega^e_m\right)^2 + \left(E_{\mathbf{l}+\mathbf{q}} - \mu\right)^2}\Delta_{\mathbf{l}+\mathbf{q},m} = \Delta_{\mathbf{q},n}, \tag{7}$$

where the fermionic Matsubara frequency is $\omega^e_m = \pi T(2m + 1)$. The angle (between $\mathbf{l}$ and $\mathbf{q}$) integration can be performed for a conventional s-wave solution (observed in experiments [27]), leading to a simplified eigenvalue problem:

$$\frac{T_c m^*}{\pi}\sum_m\frac{1}{\omega^e_m}\left\{\frac{(2\pi Ze^2)^2}{M}\frac{f_{\rm ph}(\omega^e_m/4\mu)}{\left(\omega^b_{n-m}\right)^2 + \Omega^2} - f_C\left(\frac{|\omega^e_m|}{4\mu}, \frac{|\omega^b_{n-m}|}{4\mu}\right)\right\}$$
$$\Delta_m = \Delta_n. \tag{8}$$

The integrals (over $l \equiv |\mathbf{l}|/2k_F$) for the phonon and Coulomb contributions are defined as

$$f_{\rm ph}(z) = \int_{l=0}^1 e^{-(4k_F d)l}R(z,l),$$
$$f_C(y,z) = \pi\int_{l=0}^1 R(z,l)\left\{\varepsilon(4E_F y)\frac{k_F l}{e^2} + 2m^*\left(1 + l^{-2}\sqrt{(l^2 + iy)^2 - l^2}\right)\right\}^{-1}, \tag{9}$$

where $R(z,l) = \mathrm{Re}(1 + z^2/l^2 - 2i|z| - l^2)^{-1/2}$.

Critical temperature is obtained when the largest eigenvalue of the matrix of the linear Eq. (8) is 1. This was done numerically by limiting variable n to $|n| < 200$. The numerical results are presented in Figs. 2 and 3 for values of the bulk substrate dielectric constant $30 < \varepsilon_0 < 10\,000$. The range of effective masses is $m_e < m^* < 4m_e$, while the distance (in units of the lattice spacing a) between the conducting layer and the vibrating oxygen atoms is $1 < d/a < 1.6$.

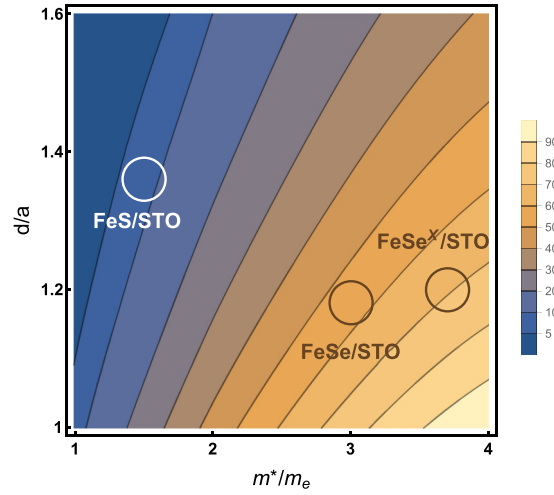

FIG. 2. Superconducting critical temperature as function of effective mass and the distance between the iron chalcogenite layer and the interface TiO_2 (where the relevant phonon modes originate). The dielectric constant $\varepsilon_0 = 3000$ is fixed to represent $SrTiO_3$.

III. RESULTS

The dependence of the critical temperature on the effective mass m^* and the distance between the 1UC iron chalcogenide and underlying TiO_2 interface layer is given in Fig. 2. It explains the dichotomy between a very high T_c in FeSe/STO and a very low T_c (10 K or less) in FeS/STO. An approximate location of the two cases is indicated by two circles. The

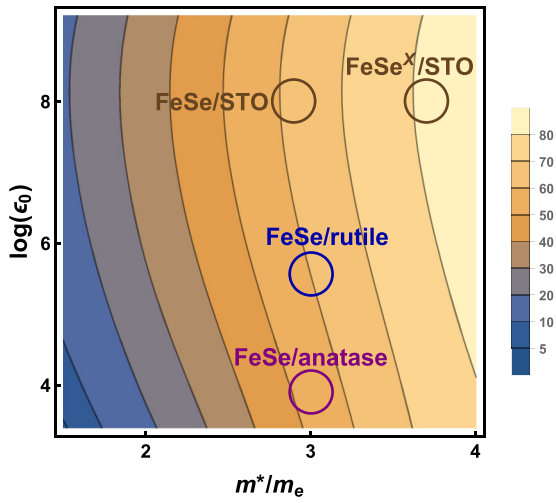

FIG. 3. Critical temperature of 1UC FeSe on ionic substrates as function of effective mass and the substrate dielectric constant ε_0 (in the logarithmic scale). The distance between the iron chalcogenide layer and the interface TiO_2 is fixed at $d = 1.1a$. Strongly dielectric substrate material STO and moderately dielectric TiO_2 forms rutile ($\varepsilon_0 = 300$) and anatase ($\varepsilon_0 = 300$) are marked.

dielectric constants are fixed on the STO values mentioned above. It demonstrates that both the reduction of the effective mass and (to a lesser degree) the distance d difference contribute to the suppression of superconductivity in FeS/STO. In addition, a higher effective mass 1UC strained FeSe epitaxially grown on Nb: $SrTiO_3/KTaO_3$ heterostructures [28] is marked as $FeSe^X$. For $T_c > 50$ K the dependence is approximately linear $T_c[\mathrm{K}] = 18\, m^*/m_e - 22\, d[\text{Å}] + 114$.

The critical temperature as function m^* of 1UC FeSe on ionic substrates with various dielectric constant is shown in Fig. 3. The ratio d/a is fixed at 1.1. Dependence on the dielectric constant is due to screening of the Coulomb interaction. The pseudopotential becomes important for low T_c. High $\varepsilon_0 = 3000$ STO and two relatively low ε forms of TiO_2, rutile, and anatase, are shown.

The effect of SF is considered in the framework of the minimal one-band model by introducing the on-site repulsion U in addition to the screened longer range Coulomb one, see details in Appendix A. The results are the following. For nonzero U, in addition to the s-wave solution (nearly independent of the angle) of the Gorkov equations, the d-wave solution with continuously changing signs appears four times. Comparing the energy of the two solutions as a function of U, one finds that the transition from the s-wave to the d-wave symmetry occurs at $U = 2t$.

IV. DISCUSSION AND CONCLUSIONS

To summarize, the dominant interfacial soft LO phonon pairing theory [8] in 1UC FeSe/STO is extended to recently fabricated iron chalcogenides FeCh (Ch = Se, S, Te) on polar insulator ($SrTiO_3$, TiO_2) substrates. In addition, to address quantitatively the dichotomy [15] between FeSe/STO and FeS/STO, the theory is refined to include the Coulomb screening and (presumably subdominant) SF effects within the electron band. The LO phonon modes originate in the ionic TiO_2 layer of the substrate adjacent to the 1UC FeCh. In contrast to other approaches concentrating on the highest frequency 100 meV modes [9], the softer 60 meV oxygen lateral vibration mode contributes the most to superconductivity. The screened Coulomb repulsion slightly reduces T_c without distortion of the plain s-wave symmetry of the order parameter. The SFs change the character of pairing at intermediate on-site repulsion $U/t > 2$. The d-wave state has lower energy than the s wave. Since available experiments favor the plain s wave, it likely that U is small in these systems.

The theory predicts the three following tendencies leading to high critical temperature T_c: To achieve high critical temperature, one requires (i) small spacing between the electron gas inside the FeCh layer and the TiO_2 interfacial layer maximizing the strength of the electron-phonon coupling, (ii) high effective mass of the electrons in FeCh maximizing density of states (DOS), and (iii) large dielectric constant ε_0 minimizing the Coulomb repulsion (pseudopotential) effects. These three effects explain why FeSe/STO has very high T_c, while FeS/STO has very low T_c, if any. In addition, it explains relative strength of pairing in FeSe on $BaTiO_3$, rutile, and anatase structures of TiO_2.

Let us put the interfacial theory of superconductivity in iron chalcogenides on ionic crystals in a more general framework of superconductivity in iron-based materials. 3D pnictides like FeAs and 3D iron chalcogenides like the parent compounds FeSe or FeS generally have two features. The superconductivity is not the plain s wave observed [27] in 1UC FeCh/TiO_2. It changes signs and is explained by the SF multiband model [5]. It is crucial that, in addition to an electron band at M, there also exists an electron band at Γ. In addition, typically, one often observes an orbital selective Mott transition further favoring an SF pairing (usually $s^{\pm}$) mechanism. It is not easy to modify these models to the plain s-wave gap typical of low T_c metals. The basic idea is still to utilize the hole pocket that is now about 100 meV below the Fermi surface [5,11,12] (the incipient band). A similar problem exists in explaining relatively high (T_c up to 48 K) superconductivity in several 3D modifications of FeCh. These materials, including [29] metal intercalated (up to 48 K) FeSe, $A_xFe_{2-y}Se_2$ (A = K, Sb, Li), and organic intercalations [30] like $Li_x(NH_2)_y(NH_3)_{1-y}Fe_2Se_2$, (Li,Fe)OHFeSe (up to 30 K) and electric field induced superconductivity (48 K) in FeSe [31], superlattice structures with alternating FeAs [32], and perovskite layers like Sr_2VO_3FeAs all exhibit s-wave pairing and only electron bands. It is plausible that bulk phonons also might provide a glue for the s-wave pairing. Therefore, the pairing glue for the three groups of superconducting materials might be different. They are interface phonons for FeSe/STO, SF for iron pnictides and parent iron chalcogenides, and either SF or 3D phonons for intercalated iron chalcogenides.

Note that often the T_c enhancement in all three kinds of systems is attributed to charging [18] of the conducting layers by either electric field or intercalation (internal pressure). As the present paper demonstrates, since in 2D the pairing depends strongly on density of states (on the Fermi level), the charging argument is only effective for 3D electron gas. In 2D, DOS depends on effective mass only, $D \propto m^*/\hbar^2$. Charging mostly

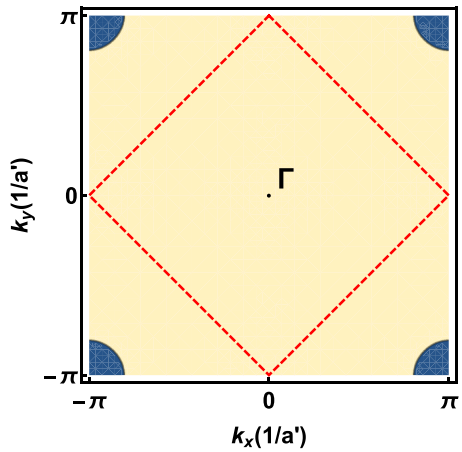

FIG. 4. The Brillouin zone of the minimal one-band model. The red dashed line is the BZ containing two Fe atoms with lattice spacing $a = \sqrt{2}a'$. The small electron pocket is nearly circular (with center at the M point).

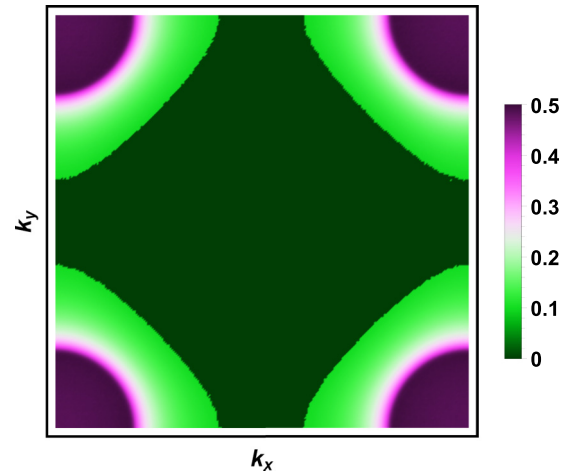

FIG. 5. The (Matsubara) static ($n = 0$) susceptibility of the electron gas with dispersion relation Eq. (A2) of the minimal model. One observes a peak near the $(\pi, \pi)/a'$ point, indicating a tendency toward antiferromagnetic correlations.

shifts the chemical potential and for fixed m^* increases DOS only in 3D: $D \propto m^{*3/2}\mu^{1/2}/\hbar^3$.

ACKNOWLEDGMENTS

We are grateful to Professor L. Wang, G. He, J.D. Guo, D. Li, J.J. Lin, and J.Y. Lin for helpful discussions. The work of B.R. was supported by National Science Council of Taiwan R.O.C. (NSC) of R.O.C. Grant No. 98-2112-M-009-014-MY3.

APPENDIX A: MINIMAL ONE-BAND MODEL FOR FeSe/FeS ON SUBSTRATES

1. Minimal one-band model

We use here the reduced unit cell with BZ of size $2\pi/a' \times 2\pi/a'$. The ARPES experiments [15] are well described (better than 5%) by the nearest-neighbor hopping,

$$H_e = \sum_{\mathbf{k}} c_{\mathbf{k}}^{\sigma\dagger}(\epsilon_{\mathbf{k}} - \mu)c_{\mathbf{k}}^{\sigma}, \tag{A1}$$

where σ is the spin index and

$$\epsilon_{\mathbf{k}} = -2t\{2 + \cos(a'k_x) + \cos(a'k_y)\}. \tag{A2}$$

One should take the hopping energy $t = 170$ meV and the Fermi energy $\mu = 60$ meV for FeSe. This will be referred to as the minimal tight-binding model describing the small (radius $k_F = \sqrt{2m^*\mu} \approx 0.6/a'$) electron pocket with effective mass $m^* = \hbar^2/(2ta'^2)$ at the M point, see Fig. 4. The pairing interactions due to interface phonons and SFs as well as the Coulomb suppression effects are addressed next.

2. The phonon-mediated effective attraction

It is important to note that the oxygen atoms in the last TiO_2 layer reside directly below Fe atoms. The dominant superconductuctivity LO phonon mode originates mainly from the lateral vibrations of these (charged) oxygen atoms that can be accounted for. Influence on the electron-phonon coupling of vibrating Ti atoms of the first layer is further reduced since they are not situated directly beneath the Fe sites. In our case, the STO surface phonon interaction with the 2DEG on the Fe layer $d = 4.4A$ above the TiO_2 plane is determined by the electric potential created near the Fe orbitals. Although the spectrum and polarization of phonons depend strongly on the sublattice, see Fig. 5 in second Ref. [8], the matrix elements of the electron-phonon coupling are not.

Indeed, expanding the electric potential in displacement using the small unit cell basis, $\mathbf{r_m} = (m_x, m_y)a'$, one obtains (Appendix B in second Ref. [8])

$$\Phi(\mathbf{r}, z) \approx \Phi^0_{e-i}(\mathbf{r}, z) - \mathrm{Ze}\sum_{\mathbf{m}} \frac{(\mathbf{r} - \mathbf{r_m})\cdot\mathbf{u_m}}{(|\mathbf{r} - \mathbf{r_m}|^2 + z^2)^{3/2}}. \tag{A3}$$

The Hamiltonian for interaction with electrons on the Fe orbitals with wave functions $\varphi_{\mathbf{l}}(\mathbf{r}, z)$, $H_{ei} = \int_{\mathbf{r}} \Phi(\mathbf{r})\widehat{n}_{\mathbf{r}}$, expanded to first order in the oxygen vibrations, thus is

$$H_{ei} = -\mathrm{Ze}^2 \int_{\mathbf{r},z} \sum_{\mathbf{m}} \frac{(\mathbf{r} - \mathbf{r_m})\cdot\widehat{\mathbf{u}}_{\mathbf{m}}}{((\mathbf{r} - \mathbf{r_m})^2 + z^2)^{3/2}} |\varphi_{\mathbf{l}}(\mathbf{r}, z)|^2 \widehat{c}_{\mathbf{l}}^{\sigma\dagger}\widehat{c}_{\mathbf{l}}^{\sigma}. \tag{A4}$$

Although the most general matrix element also depends on the electron momentum $\mathbf{k}$ in addition to the phonon momentum $\mathbf{q}$, it does not appear in Eq. (A4) since the coupling is to the density, namely, the size of the Fe orbital is neglected. Indeed, in the localized form, namely, neglecting the size of the orbital, $|\varphi_{\mathbf{l}}(\mathbf{r}, z)|^2 = \delta(\mathbf{r} - \mathbf{r_l})\delta(z - d)$, one obtains

$$H_{ei} = -\mathrm{Ze}^2 \sum_{\mathbf{l},\mathbf{m}} \frac{(\mathbf{r_l} - \mathbf{r_m})\cdot\widehat{\mathbf{u}}_{\mathbf{m}}}{((\mathbf{r}_l - \mathbf{r_m})^2 + d^2)^{3/2}} \widehat{n}_{\mathbf{l}}. \tag{A5}$$

Performing the Fourier transformation,

$$\mathbf{u_m} = \frac{1}{N}\sum_{\mathbf{k}} \mathbf{u_k} e^{ia'\mathbf{k}\cdot\mathbf{m}},$$
$$n_{\mathbf{l}} = \frac{1}{N}\sum_{\mathbf{k}} n_{\mathbf{k}} e^{ia'\mathbf{k}\cdot\mathbf{l}}, \tag{A6}$$

the electron-phonon Hamiltonian becomes

$$H_{ei} = -\frac{\mathrm{Ze}^2}{a'^2}\sum_{\mathbf{k}} g^{\alpha}_{\mathbf{k}} u^{\alpha}_{\mathbf{k}} n_{-\mathbf{k}}. \tag{A7}$$

Here the electron-phonon matrix element has the form

$$g^{\alpha'}_{\mathbf{k}} = \sum_{\mathbf{m}} \frac{m^{\alpha}}{(\mathbf{m}^2 + d^2/a'^2)^{3/2}} e^{i\mathbf{k}\cdot\mathbf{r}_{\mathbf{m}}}. \tag{A8}$$

The electron-phonon contribution to the Matsubara action in the functional approach therefore is

$$\mathcal{A}_{\mathrm{e-ph}}[\psi, u] = \frac{\mathrm{Ze}^2}{\mathrm{Ta}'^2}\sum_{\mathbf{k},n} g^{\alpha}_{\mathbf{k}} u^{\alpha}_{\mathbf{k},n} n_{-\mathbf{k},-\mathbf{n}}, \tag{A9}$$

which will be used below. Here $\psi^{\sigma}_{\mathbf{k},n}$ is a complex Grassmann field describing electronic degrees of freedom, while $u^{\alpha}_{\mathbf{k},n}$ is the displacement field.

In addition to the electron-phonon coupling, the action contains the electron and the phonon (see Ref. [8]) parts:

$$\mathcal{A}_e[\psi] = T^{-1}\sum_{\mathbf{k},n} \psi^{*\sigma}_{\mathbf{k},n}\left(G^0_{\mathbf{k},n}\right)^{-1}\psi^{\sigma}_{\mathbf{k},n},$$

$$\mathcal{A}_{\mathrm{ph}}[u] = \frac{M}{2T}\sum_{\mathbf{k},n} u^{\alpha}_{-\mathbf{k},-n}\Pi^{\alpha\beta}_{\mathbf{k},n} u^{\beta}_{\mathbf{k},n}. \tag{A10}$$

Here the (bare) Green's function for normal electrons is

$$G^0_{\mathbf{k},n} = \left(i\omega^f_n - \epsilon_{\mathbf{k}} + \mu\right)^{-1}, \tag{A11}$$

with $\omega^f_n = \pi T(2n+1)$. The 2D polarization tensor is defined via the dynamic matrix $D_{\mathbf{q}}$ calculated from a microscopic theory,

$$\Pi^{\alpha\beta}_{\mathbf{q},n} = \left(\omega^b_n\right)^2\delta_{\alpha\beta} + M^{-1}D^{\alpha\beta}_{\mathbf{q}}, \tag{A12}$$

Here $\omega^b_n = 2\pi nT$ is the Matsubara frequency for phonons.

Since the action in Eqs. (A10) is quadratic in the displacement field $\mathbf{u}$, the electronic effective action is obtained by the Gaussian integration over the field:

$$e^{-\mathcal{A}^{\mathrm{ph}}_{\mathrm{eff}}[\psi]} = \int_u e^{-\mathcal{A}_{ph}[u]-\mathcal{A}_{\mathrm{eph}}[\psi,u]}. \tag{A13}$$

As a result, one obtains an effective electron-electron interaction term,

$$\mathcal{A}^{\mathrm{ph}}_{\mathrm{eff}} = \frac{1}{2T}\sum_{\mathbf{k}.n} n_{\mathbf{k},n} v^{\mathrm{ph}}_{\mathbf{k},n} n_{-\mathbf{k},-n}, \tag{A14}$$

where the effective dynamical potential for soft LO phonon mode is

$$v^{\mathrm{ph}}_{\mathbf{q},n} = -\frac{(\mathrm{Ze}^2)^2}{2M}\frac{g_{\mathbf{k}}g_{-\mathbf{k}}}{\omega^{b2}_n + \Omega^2_{\mathbf{k}}}, \tag{A15}$$

where, for the longitudinal polarization $\mathbf{e}_{\mathbf{k}}$, an excellent approximation (2%) exists:

$$g_{\mathbf{k}} = \mathbf{e}_{\mathbf{k}}\cdot\mathbf{g}_{\mathbf{k}} = \frac{2\pi}{a'^2}e^{-q_{\mathrm{lat}}d}. \tag{A16}$$

Here the function

$$q_{\mathrm{lat}} = \frac{2}{a'}\sqrt{\sin^2(k_x a'/2) + \sin^2(k_y a'/2)} \tag{A17}$$

is periodic on the BZ. This is consistent with the continuum limit expression used in Eq. (1) of the text for the efficient T_c evaluation.

3. Coulomb repulsion and its screening

The Coulomb repulsion (with screening on the atomic level taken into account) can be separated into the on-site and the longer range contribution terms of the lattice Hamiltonian:

$$H^C_{e-e} = H^S_{e-e} + H^L_{e-e}. \tag{A18}$$

The short-range part is described by the Hubbard repulsion term,

$$H^S_{e-e} = U\sum_{\mathbf{n}} n^{\uparrow}_{\mathbf{n}} n^{\downarrow}_{\mathbf{n}}, \tag{A19}$$

while the long range repulsion has a form

$$H^L_{e-e} = \frac{1}{2}\sum_{\mathbf{n}\neq\mathbf{m}} U_{\mathbf{n}-\mathbf{m}} n_{\mathbf{n}} n_{\mathbf{m}}, \tag{A20}$$

with $n_{\mathbf{n}} = c^{\uparrow\dagger}_{\mathbf{n}}c^{\uparrow}_{\mathbf{n}} + c^{\downarrow\dagger}_{\mathbf{n}}c^{\downarrow}_{\mathbf{n}}$ on the site (n_x, n_y).

The longer range Coulomb potential can be obtained by Wannier transformation, where $\mathbf{k}$ is the crystal momentum. In this case, the action becomes

$$\mathcal{A}^L = \frac{1}{2T}\sum_{\mathbf{k},n} V^C_{\mathbf{k},n} n_{-\mathbf{k},n} n_{\mathbf{k},n}, \tag{A21}$$

where using the random phase approximation (RPA) obtain for the effective long-range Coulomb contribution in the presence of the semi-infinite dielectric slab is

$$V^C_{\mathbf{k},n} = \frac{v^C_{\mathbf{k},n}}{1 - 2v^C_{\mathbf{k},n}\chi_{k_{\mathrm{lat}},n}}, \quad v^C_{\mathbf{k},n} = \frac{2\pi}{\varepsilon(\omega_n)k_{\mathrm{lat}}}. \tag{A22}$$

The dynamical dielectric function ε due to the substrate given in Eq. (4) of the text and $\chi_{\mathbf{k},n}$ is the polarization fish diagram,

$$\chi_{\mathbf{k},n} = \frac{2}{(2\pi)^2}\int_{\mathrm{BZ}} d^2q \frac{n_F(\epsilon_{\mathbf{q}}) - n_F(\epsilon_{\mathbf{k}+\mathbf{q}})}{i\omega_n + \epsilon_{\mathbf{q}} - \epsilon_{\mathbf{k}+\mathbf{q}}}, \tag{A23}$$

where n_F is the Fermi distribution function. The function is proportional to the spin susceptibility that plays an important role in the SF pairing and is given at zero Matsubara frequency in Fig. 2.

Note that it has maxima near the crystallographic M point expressing a tendency to antiferromagnetic correlations. In the continuum limit (away from the BZ boundaries), it coincides with the exactly calculated integral that reads

$$\chi_{\mathbf{k},n} = -\frac{m^*}{\pi}\left\{1 + 2\,\mathrm{Re}\sqrt{(1/2 + i\omega_n m^*/k^2)^2 - (k_F/k)^2}\right\}. \tag{A24}$$

The short-range repulsion should be treated differently. In principle, it could be effective d-wave pairing [33] due to the SF exchange already appearing in the second order in U.

4. Effective electron-electron interaction due to the spin fluctuations

The second order in U contribution [34] to the effective action (keeping only terms relevant to the singlet pairing) is

$$\mathcal{A}^S = \frac{1}{2T}\sum_{\mathbf{k},\mathbf{l},n,m}\left(U + U^2 v^S_{\mathbf{k}+\mathbf{l},n+m}\right) \times \psi^{\dagger\uparrow}_{\mathbf{l},n}\psi^{\uparrow}_{-\mathbf{l},-n}\psi^{\uparrow}_{-\mathbf{k},-m}\psi^{\uparrow}_{\mathbf{k},m} + \text{c.c.} \tag{A25}$$

The second term represents the SF exchange can be represented for sufficiently small U (with RPA/FLEX (fluctuation exchange approximation)-type improvements possible [33,35]). The effective electron-electron interaction consists of all these contributions:

$$v^S_{\mathbf{k},n} = U + U^2\chi_{\mathbf{k},n}. \tag{A26}$$

This potential is next used to develop the (Eliashberg) theory of superconductivity along with the phonon and the long-range Coulomb contributions given in Eqs. (A15) and (A22).

APPENDIX B: SYMMETRY OF THE ORDER PARAMETER

1. Gap equation

The STM experiments [27] demonstrate that the order parameter is gapped (hence no nodes) and indicate a weakly anisotropic spin singlet pairing. Therefore, we look for solutions for the normal and the anomalous Green's function of the Gorkov equations in the form

$$\left\langle c^{\rho}_{\mathbf{k},n}c^{\dagger\sigma}_{\mathbf{k},n}\right\rangle = \delta^{\sigma\rho}G_{\mathbf{k},n};\ \left\langle c^{\sigma}_{\mathbf{k},n}c^{\rho}_{-\mathbf{k},-n}\right\rangle = \varepsilon^{\sigma\rho}F_{\mathbf{k},n}, \tag{B1}$$

where $\varepsilon^{\sigma\rho}$ is the antisymmetric tensor.

Gorkov equations (index α combines momenta and frequencies) are

$$\begin{aligned} G_\alpha\left(G^0_\alpha\right)^{-1} + F_\alpha\Delta^*_\alpha &= 1,\\ G_\alpha\Delta_\alpha + F_\alpha G^0_{-\alpha} &= 0, \end{aligned} \tag{B2}$$

and the gap function is defined as

$$\Delta_\alpha = -\sum_\chi v_{\alpha-\chi}F_\chi. \tag{B3}$$

The corresponding gap equation is

$$\Delta_{\mathbf{k},n} = -\sum_{\mathbf{p},m}\frac{v_{\mathbf{k}-\mathbf{p},n-m}\Delta_{\mathbf{p},m}}{\omega^{f2}_m + (\epsilon_{\mathbf{p}}-\mu)^2 + |\Delta_{\mathbf{p},m}|^2}. \tag{B4}$$

The condensation energy density (subtracting the normal state energy) is

$$\Phi[\Delta] = \sum_{\mathbf{k},n}\left\{\begin{array}{c} -\ln\left[\frac{\omega^{f2}_n+(\epsilon_{\mathbf{k}}-\mu)^2+|\Delta_{\mathbf{k},n}|^2}{\omega^{f2}_n+(\epsilon_{\mathbf{k}}-\mu)^2}\right] \\ -\frac{1}{2}\left(\frac{\omega^{f2}_n+(\epsilon_{\mathbf{k}}-\mu)^2-|\Delta_{\mathbf{k},n}|^2}{\omega^{f2}_n+(\epsilon_{\mathbf{k}}-\mu)^2+|\Delta_{\mathbf{k},n}|^2}-1\right)\end{array}\right\}. \tag{B5}$$

This expression will be used to compare different pairing channels.

2. The pairing symmetry dependence on U

Equation (B4) was solved for the Matsubara gap function Δ by iterations starting either from an s-wave or d-wave configuration. The BZ was discretized by 256×256 points with 128 Matsubara frequencies. We make an extensive use of fast Fourier transform [36]. It is important to note that for relatively large U there is a difference between the gap function Δ and the anomalous Green's function F, see Eq. (B3). We therefore invert this equation (by multiple fast Fourier transforms) to obtain F.

Typical solutions for the 1UC FeSe/STO gap functions and the order parameters correlator F are presented in Figs. 6–8. The distribution of the order anomalous correlator (the order parameter) F for $n=0$ is shown.

One observes that the parameter is concentrated in a narrow shell around the Fermi surface of Fig. 4. As expected, while the s-wave solution is nearly independent of the angle, the d-wave solution continuously changes signs four times. The d-wave solutions of the five-band band model for nonzero U were found recently in Ref. [11]. To more conveniently com-

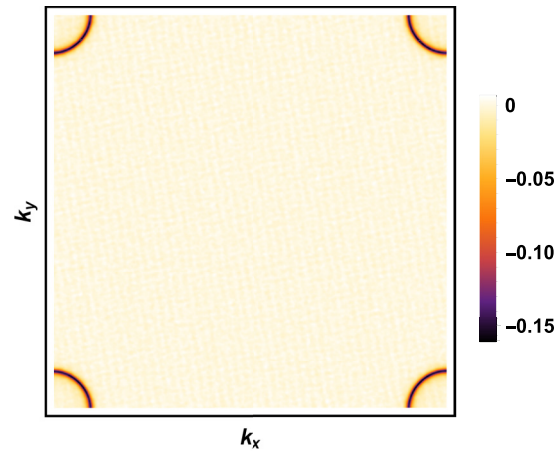

FIG. 6. The ($n=0$ Matsubara) gap function for the s-wave solution of Eq. (B4). One observes that the function is concentrated in a narrow shell near the Fermi surface, see Fig. 4.

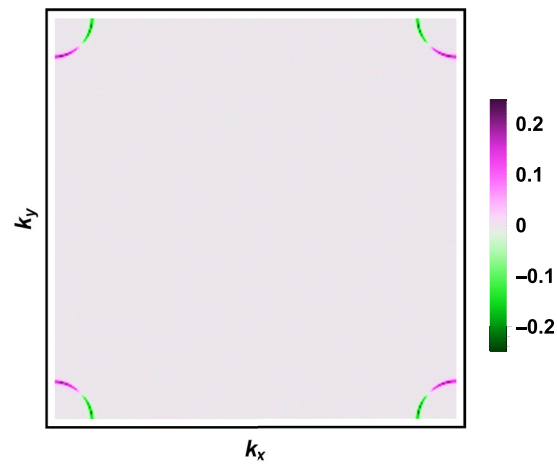

FIG. 7. The anomalous average (order parameter) F defined in Eq. (B1) for the d-wave solution at the on site repulsion $U=2t$. Note that, as for the s wave, it is concentrated in the narrow shell around the Fermi surface. The correlator continuously changes signs four times.

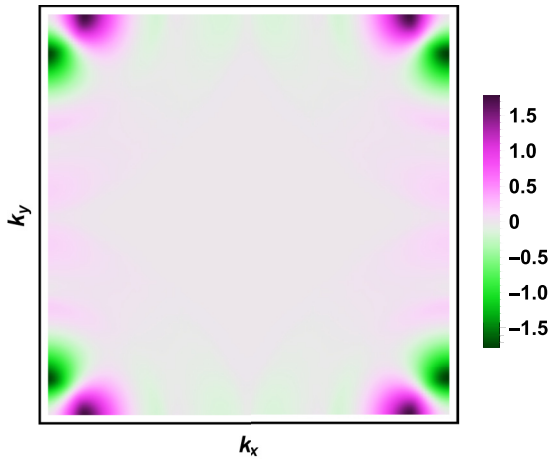

FIG. 8. The (Matsubara) gap function Δ defined in Eq. (B3) for the d-wave solution at $U = 2t$. Note that due to the on-site repulsion term, this.quantity spreads over beyond the narrow shell around the Fermi surface.

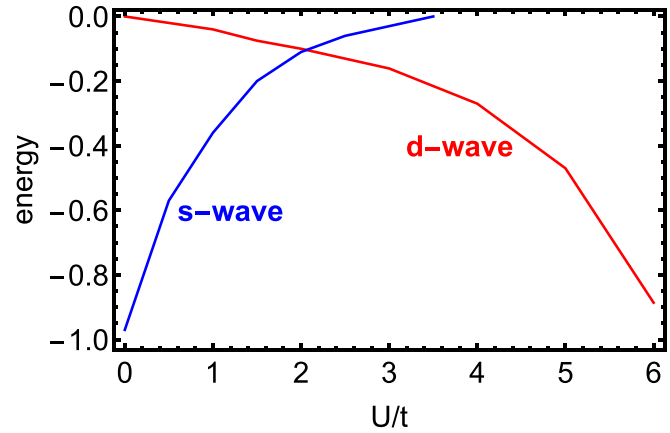

FIG. 9. Comparison of energies of the s- and d-wave solutions for various values of the on-site repulsion U. The transition occurs at $U = 2t$.

pare with it, the Matsubara gap function is given in Fig. SM5. The gap function is smeared away from the Fermi function compared to Fig. SM4. It differs considerably from Fig. 1 of first Ref. [11].

The energy, Eq. (B5), of the two solutions as a function of U are plotted in Fig. 9. It shows that the transition from the s-wave to the d-wave symmetry occurs at $U = 2t$. One can question the applicability of the SF exchange given by Eq. (A26) for an intermediate range U. Apparently, even including the RPA enhancement, the results are similar, see Ref. [11] in which the absolute value of the gap function was compared for the s-wave and d-wave solutions.

3. The tight-binding model versus the continuum limit (the effective mass approximation)

The fact that the order parameter is concentrated near the Fermi surface, see Fig. 6, supports the simplified s-wave approach employed in the text in which the correlator is taken at $|\mathbf{k}| = k_F$. This is not evident for the system under consideration since it is not strongly adiabatic. The phonon energy $\hbar\Omega = 60\,\text{meV}$ is actually of the same order as the Fermi energy $\mu = 60\,\text{meV}$.

The critical temperature was estimated in the lattice model by vanishing the Matsubara gap function. The results in the whole range of parameters coincide with a much simpler calculation described in the text to within 3%.

[1] Q.-Y. Wang, Z. Li, W.-H. Zhang, Z.-C. Zhang, J.-S. Zhang, W. Li, H. Ding, Y-B. Ouu, P. Deng, and K. Chang, Chin. Phys. Lett. **29**, 037402 (2012); D. Liu, S. He, J. He, W. Zhang, L. Zhao, D. Liu, X. Liu, D. Mou, Y.-B. Ou, Q.-Y. Wang, Z. Li, L. Wang *et al.*, Nat. Com. **3**, 931 (2012); S. He, W. Zhang, D. Mou, J. He, Y.-B. Ou, Q.-Y. Wang, Z. Li, L. Wang, L. Zhao, S. He *et al.*, Nat. Mater. **12**, 605 (2013); Q. Wang, W. Zhang, W. Chen, Y. Xing, Y. Sun, Z. Wang, J.-W. Mei, Z. Wang, L. Wang, and X.-C. Ma, 2D Mater. **2**, 044012 (2015).

[2] S. N. Rebec, T. Jia, C. Zhang, M. Hashimoto, D.-H. Lu, R. G. Moore, and Z.-X. Shen, Phys. Rev. Lett. **118**, 067002 (2017).

[3] H. Ding, Y. F. Lv, K. Zhao, W. L. Wang, L. Wang, C. L. Song, X. Chen, X. C. Ma, and Q. K. Xue, Phys. Rev. Lett. **117**, 067001 (2016).

[4] R. Peng, H. C. Xu, S. Y. Tan, H. Y. Cao, M. Xia, X. P. Shen, Z. C. Huang, C. H. P. Wen, Q. Song, T. Zhang *et al.*, Nat. Com. **5**, 5044 (2014).

[5] A. Kreisel, P. J. Hirschfeld, and B. M. Andersen, Symmetry **12**, 1402 (2020); F. Schrodi, A. Aperis, and P. M. Oppeneer, Phys. Rev. B **102**, 014502 (2020); R. Yu, H. Hu, E. M. Nica, J.-X. Zhu, and Q. Si, Front. Phys. **9**, 578347 (2021).

[6] A. Linscheid, S. Maiti, Y. Wang, S. Johnston, and P. J. Hirschfeld, Phys. Rev. Lett. **117**, 077003 (2016).

[7] Q. Song, T. L. Yu, X. Lou, B. P. Xie, H. C. Xu, C. H. P. Wen, Q. Yao, S. Y. Zhang, X. T. Zhu, J. D. Guo *et al.*, Nat. Com. **10**, 758 (2019).

[8] B. Rosenstein, B. Y. Shapiro, I. Shapiro, and D. Li, Phys. Rev. B **94**, 024505 (2016); B. Rosenstein and B. Ya. Shapiro, *ibid.* **100**, 054514 (2019).

[9] L. Rademaker, Y. Wang, T. Berlijn, and T. Johnston, New J. Phys. **18**, 022001 (2016); Y. Wang, K. Nakatsukasa, L. Rademaker, T. Berlijn, and S. Johnston, Supercond. Sci. Technol. **29**, 054009 (2016).

[10] M. L. Kulić and O. V. Dolgov, New J. Phys. **19**, 013020 (2017); M. L. Kulić, Phys. Rep. **38**, 1 (2000).

[11] F. Schrodi, A. Aperis, and P. M. Oppeneer, Phys. Rev. B **102**, 180501(R) (2020); L. Rademaker, G. Alvarez-Suchini, K. Nakatsukasa, Y. Wang, and S. Johnston, *ibid.* **103**, 144504 (2021)

[12] Y. Bang, Sci. Rep. **9**, 3907 (2019).

[13] S. Zhang, J. Guan, X. Jia, B. Liu, W. Wang, F. Li, L. Wang, X. Ma, Q. Xue, J. Zhang *et al.*, Phys. Rev. B **94**, 081116(R) (2016); S. Zhang, J. Guan, Y. Wang, T. Berlijn, S. Johnston, X. Jia, B. Liu, Q. Zhu, Q. An, S. Xue *et al.*, *ibid.* **97**, 035408 (2018); X. Xu, S. Zhang, X. Zhu, and J. Guo, J. Phys. Cond. Mat. **32**, 343003 (2020).

[14] J. Pelliciari, S. Karakuzu, Q. Song, R. Arpaia, A. Nag, M. Rossi, J. Li, T. Yu, X. Chen, R. Peng *et al.*, Evolution of spin excitations from bulk to monolayer FeSe, arXiv:2008.09618 v1.

[15] K. Shigekawa, K. Nakayama, M. Kuno, G. N. Phana, K. Owada, K. Sugawara, T. Takahashi, and T. Sato, PNAS **116**, 24470 (2019).

[16] D. Liu, Xianxin Wu, Fangsen Li, Yong Hu, Jianwei Huang, Yu Xu, Cong Li, Yunyi Zang, Junfeng He, Lin Zhao *et al.* Origin of the electronic structure in single-layer FeSe/$SrTiO_3$ films, arXiv:2012.09032.

[17] F. Li, Q. Zhang, C. Tang, C. Liu, J. Shi, C. N. Nie, G. Zhou, Z. Li, W. Zhang, and C.-L. Song, 2D Mater. **3**, 024002 (2016).

[18] L. Wang, X. Ma, and Q.- K. Xue, Supercond. Sci. Technol. **29**, 123001 (2016).

[19] A. Aperis and P. M. Oppeneer, Phys. Rev. B **97**, 060501(R) (2018).

[20] N. Hao and J. Hu, Phys. Rev. X **4**, 031053 (2014).

[21] S. Graser, T. A. Maier, P. J. Hirschfeld, and D. J. Scalapino, New J. Phys. **11**, 025016 (2009).

[22] L. P. Gorkov, Phys. Rev. B **93**, 060507(R) (2016).

[23] F. Li and G. A. Sawatzky, Phys. Rev. Let. **120**, 237001 (2018).

[24] L. Zhao, A. Liang, D. Yuan, Y. Hu, D. Liu, J. Huang, S. He, B. Shen, Y. Xu, X. Liu *et al.*, Nat. Commun., **7**, 10608 (2016); B. Li, Z. W. Xing, G. Q. Huang, and D. Y. Xing, J. Appl. Phys. **115**, 193907 (2014); Y. Wang, A. Linscheid, T. Berlijn, and S. Johnston, Phys. Rev. B **93**, 134513 (2016).

[25] R. A. Evarestov, *Quantum Chemistry of Solids*, 2nd ed., Springer Series in Solid-State Sciences (Springer, London, 2012), Vol. 153.

[26] W. L. McMillan, Phys. Rev. **167**, 331 (1968).

[27] Q. Fan, W. H. Zhang, X. Liu, Y. J. Yan, M. Q. Ren, R. Peng, H. C. Xu, B. P. Xie, J. P. Hu, T. Zhang *et al.*, Nat. Phys. **11**, 946 (2015); C. Tang, C. Liu, G. Zhou, F. Li, H. Ding, Z. Li, D. Zhang, Z. Li, C. Song, S. Ji *et al.*, Phys. Rev. B **93**, 020507(R) (2016).

[28] R. Peng, X. P. Shen, X. Xie, H. C. Xu, S. Y. Tan, M. Xia, T. Zhang, H. Y. Cao, X. G. Gong, J. P. Hu *et al.*, Phys. Rev. Lett. **112**, 107001 (2014).

[29] J. G. Guo, S. F. Jin, G. Wang, S. C. Wang, K. X. Zhu, T. T. Zhou, M. He, and X. L. Chen, Phys. Rev. B **82**, 180520(R) (2010); A. F. Wang, J. J. Ying, Y. J. Yan, R. H. Liu, X. G. Luo, Z. Y. Li, X. F. Wang, M. Zhang, G. J. Ye, P. Cheng *et al.*, *ibid.* **83**, 060512(R) (2011); M. Z. Shi, N. Z. Wang, B. Lei, C. Shang, F. B. Meng, L. K. Ma, F. X. Zhang, D. Z. Kuang, and X. H. Chen, Phys. Rev. Mater. **2**, 074801 (2018).

[30] M. Burrard-Lucas, D. G. Free, S. J. Sedlmaier, J. D. Wright, S. J. Cassidy, Y. Hara, A. J. Corkett, T. Lancaster, P. J. Baker, S. J. Blundell *et al.*, Nat. Mater. **12**, 15 (2013); X. F. Lu, N. Z. Wang, H. Wu, Y. P. Wu, D. Zhao, X. Z. Zeng, X. G. Luo, T. Wu, W. Bao, G. H. Zhang *et al.*, *ibid.* **14**, 325 (2015).

[31] B. Lei, J. H. Cui, Z. J. Xiang, C. Shang, N. Z. Wang, G. J. Ye, X. G. Luo, T. Wu, Z. Sun, and X. H. Chen, Phys. Rev. Let. **116**, 077002 (2016).

[32] H. Ogino, Y. Katsura, S. Horii, K. Kishio, and J. Shimoyama, Supercond. Sci. Technol. **22**, 085001 (2009); X. Zhu, F. Han, G. Mu, P. Cheng, B. Shen, B. Zeng, and H.-H. Wen, Phys. Rev. B **79**, 220512(R) (2009).

[33] P. Monthoux and D. J. Scalapino, Phys. Rev. Lett. **72**, 1874 (1994).

[34] W. Kohn and J. M. Luttinger, Phys. Rev. Let. **15**, 526 (1965).

[35] A. T. Rø mer, T. A. Maier, A. Kreisel, I. Eremin, P. J. Hirschfeld, and B. M. Andersen, Phys. Rev. Res. **2**, 013108 (2020).

[36] B. Rosenstein and B. Ya. Shapiro, J. Phys. Commun. **5**, 055013 (2021).